# Helicity segregation by Ekman pumping in laminar rotating flows with gravity orthogonal to rotation

Abhilash Ojha,[1,*] Mohammad Anas,[1,†] Avishek Ranjan,[2,‡] Pranav Joshi,[1,§] and Mahendra K. Verma[3,‖]

[1]*Department of Mechanical Engineering, Indian Institute of Technology, Kanpur 208016, India*
[2]*Department of Mechanical Engineering, Indian Institute of Technology Bombay, Mumbai 400076 India*
[3]*Department of Physics, Indian Institute of Technology, Kanpur 208016, India*

(Received 17 October 2021; accepted 22 February 2022; published 15 March 2022)

Kinetic helicity in most geodynamo simulations has a distinct distribution above and below the equator—it is negative in the north and positive in the south. Using direct numerical simulations of rotating convection, with the rotation axis perpendicular to gravity, we investigate the role of Ekman pumping as a possible mechanism behind this helicity segregation. For a fixed Rayleigh number $\mathrm{Ra} = 10^5$ and Prandtl number $\mathrm{Pr} = 1$, we consider two values of Taylor number, $\mathrm{Ta} = 10^5$ and $10^6$, and two different boundary conditions, no-slip and fixed stress at the walls normal to the rotation axis. We observe cyclonic flow in the bulk and helical flow driven by Ekman pumping near the boundaries normal to the rotation axis. This leads to helicity being negative (positive) near the wall with outward normal parallel (antiparallel) to the rotation vector. The peak in helicity (averaged in the plane normal to the rotation axis) occurs inside the Ekman layer in all simulations. The helicity magnitude is smaller for the fixed stress boundary condition as compared to no-slip. We also observe that the buoyancy causes the large helicity regions inside the Ekman boundary layer to migrate away from the rotation axis. We also present the helicity budget analysis, with the contribution of Coriolis force, pressure vorticity, buoyancy force, and viscosity in the helicity segregation. We find that both pressure vorticity and Coriolis force contribute significantly to the helicity segregation. Moreover, from modal energy analysis we find that the mode (2, 2), which represents the secondary flows, is important for the helicity segregation.

DOI: 10.1103/PhysRevFluids.7.034801

## I. INTRODUCTION

Helicity plays an important role in the generation of the magnetic field in planets, stars, and other celestial objects [1–5]. Helicity, or helicity density [6], is defined as $h = \mathbf{u} \cdot \boldsymbol{\omega}$, where $\mathbf{u}$ is velocity and $\boldsymbol{\omega} = \boldsymbol{\nabla} \times \mathbf{u}$ is vorticity. The Earth's core is a complex system where several forces interact—buoyancy force due to thermal and compositional gradients, Lorentz force due to the magnetic field, and Coriolis force due to the rapid rotation. The presence of helicity in the flow leads to a "lift and twist" mechanism of field generation, also called the mean-field $\alpha$ effect [1,7]. The $\alpha^2$-dynamo model, in which the $\alpha$ effect acts twice, predicts an Earth-like dipolar magnetic field, but

*abhiojha@iitk.ac.in
†anas@iitk.ac.in
‡avishekr@iitb.ac.in
§jpranavr@iitk.ac.in
‖mkv@iitk.ac.in

 

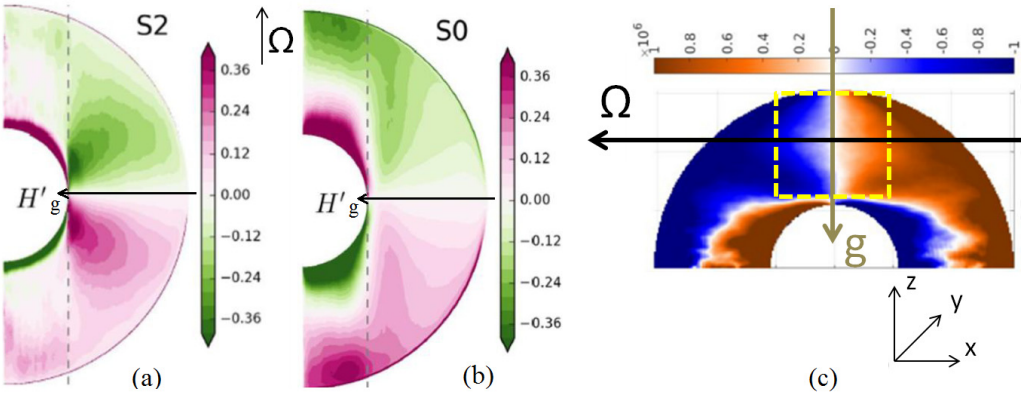


FIG. 1. (a), (b) $\phi, t$-averaged helicity calculated using the fluctuating components of velocity and vorticity from [12]. Note that Taylor number (Ta) for S0 and S2 is $4 \times 10^{10}$ and $4 \times 10^{14}$, respectively. (c) Rotated image of $\phi, t$-averaged helicity from [14] along with a Cartesian box shown in yellow near the equator, as a motivation for our simulation domain. Images are used with the permission of the authors.

it relies on the sign of helicity being negative in the north and positive in the south [8,9]. Indeed, this segregation of helicity outside the tangent cylinder is a robust feature of most dynamo simulations [8,10–14]; for instance, see Fig. 1, which contains helicity plots generated by [12,14]. However, the mechanisms of helicity generation and segregation in these dynamo simulations remain unclear and debated.

Possible mechanisms of helicity generation in dynamos were first proposed by Busse [15,16], who suggested three sources: (1) spatial variations in the Lorentz forces, (2) $\beta$ effect due to the curvature of the spherical shell, and (3) Ekman pumping near the boundaries. Though the Lorentz force may lead to local intensification or reduction in helicity [11,13], it is unlikely to create the observed segregation since the same is observed in nonmagnetic rotating convection simulations as well [8,14,17]. Similarly, the $\beta$ effect [10,18–20] can also lead to additional negative helicity in the north and positive helicity in the south due to the conservation of angular momentum, but is unlikely to cause it. Ekman pumping arises from mass conservation and an imbalance between the pressure forces and Coriolis forces near boundaries with nonzero wall shear stress. This can lead to the generation as well as segregation of negative (positive) helicity in the north (south) of the equator. However, in the Earth's core, where Taylor number Ta $\sim 10^{27}$ [21], Ekman pumping is considered to be relatively unimportant [22], here the Taylor number (Ta) signifies the importance of Coriolis force relative to the viscous force. However, most simulations are still far from the core parameter regime and are too viscous, with the closest ones at Ta $\sim 10^{14}$ [12]. In simulations with lower values of Ta, it is a matter of debate whether the helicity indeed arises due to Ekman pumping or not. For instance, in spherical magnetoconvection simulations performed at Ta $= 4.4 \times 10^7$ and Ra $= 3.1 \times 10^5$, Olson *et al.* [8] did observe helicity segregation but noted that Ekman pumping was unlikely to be important as the peak $|h|$ was far from the boundaries. Here Ra denotes the Rayleigh number that represents the strength of buoyancy forces over viscous and thermal diffusion. In yet another simulation at Ta $= 4 \times 10^8$ and Ra $= 7.5 \times 10^6$ from the same study, the helicity signs were observed to be reversed in the Ekman layer, while remaining unchanged in the bulk. They also hinted at the possible role of buoyancy in helicity generation and segregation. Recently, it was shown that the helicity source due to buoyancy was indeed positively correlated with the helicity itself in moderately forced dynamo simulations [14]. The authors speculated on the possible role of inertial waves [23,24] and their interplay with buoyancy forces.

Schaeffer *et al.* [12] reported dynamo simulations performed at some of the extreme parameter regimes that are computationally feasible with modern computing resources. Azimuthally averaged

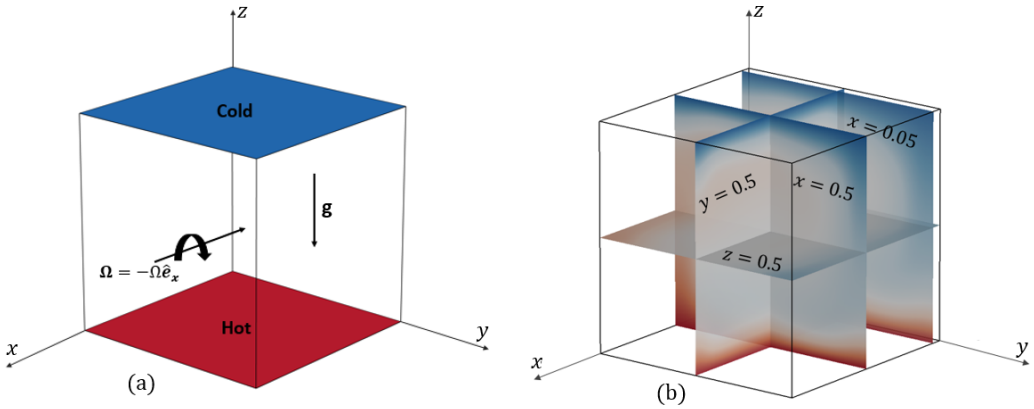


FIG. 2. (a) Schematic diagram of the model for our simulations, (b) Location of various planes in the domain.

and time-averaged helicity plots for two of their numerical dynamos are shown in Fig. 1(a): S2 ($\mathrm{Ta} = 4 \times 10^{14}$, $\mathrm{Ra} = 2.5 \times 10^{12}$) and Fig. 1(b): S0 ($\mathrm{Ta} = 4 \times 10^{10}$, $\mathrm{Ra} = 6.3 \times 10^{9}$). In both cases, there is a clear segregation of helicity, but the locations of the peak $|h|$ are different. For S2, the peak $|h|$ is in the interior (or far from boundaries), whereas for S0, the peak is closer to the boundaries. Schaeffer *et al.* [12] suggest that helicity in S0 comes most likely from Ekman pumping at the boundaries, whereas in S2 the primary source is different. However, the peak $|h|$ closer to the Ekman boundary layer observed in S0 may be contrasted with the helicity distribution in the Case 1 simulation considered by Olson *et al.* [8], which has 100 times lower Ta. The ratio Ra/Ta, which signifies the importance of buoyancy force relative to the viscous and Coriolis forces (very similar to the convective Rossby number of Aurnou *et al.* [25] or modified Rayleigh number of Christensen [26]), for the run S2 of Schaeffer *et al.* [12] and for Case 1 in Olson *et al.* [8], is approximately the same (∼0.006–0.007). Recall that for both these simulations, the peak $|h|$ lies in the interior, unlike S0 for which Ra/Ta ∼ 0.16. This indicates that perhaps it is the relative strengths of the buoyancy and the Coriolis forces that dictate the helicity distribution. Also, it remains unclear if helicity generation by Ekman pumping can be influenced by the presence of buoyancy force. This is harder to predict for the regions near the equator where gravity and rotation vector are orthogonal. The role of boundary conditions also remains unclear, since the same sign of helicity is observed even for the free-slip boundary condition for which Ekman pumping is absent [10,18,27,28]. Moreover, some researchers (e.g., Olson *et al.* [8], Sreenivasan and Jones [11]) observed the helicity magnitudes to be reduced when they adopted free-slip boundary condition.

In this study, we investigate the helicity generation and segregation due to Ekman pumping. We choose a configuration inspired by the equatorial regions of the core—a Cartesian box with rotation axis perpendicular to gravity. This nonclassical configuration has not been studied in detail, but has been of interest lately [23,24]. Moreover, helicity segregation due to the secondary flows predicted by Busse [16] and Olson *et al.* [8] has not been investigated and demonstrated to our knowledge. Our simulation domain, the Cartesian box, is shown in Fig. 2(a) for which gravity points along $-z$ and rotation along $-x$; this may be qualitatively compared with a square shown by yellow dashed lines in Fig. 1(c). We also examine the effect of boundary conditions using both no-slip and constant (nonzero) stress boundary conditions on the walls normal to the rotation axis ($yz$ planes). We also conduct modal analysis to quantify the importance of secondary flows with respect to the bulk flow, and present the force balance inside and outside the Ekman layers. The paper is organized as follows. In Sec. II we describe the numerical methodology. We present and explain our results in Sec. III. Finally, we conclude the paper in Sec. IV.

TABLE I. Simulation details: $N$ is the number of grid points in each direction and Pr = 1 for all the runs. For RCS, no-slip boundary conditions are imposed at all the walls except $x = 0$ and $x = 1$. Note that Ra $\gtrsim$ 10Ra$_c$ in RC1 and RC2, where Ra$_c$ is the critical Rayleigh number for the onset of convection.

| Run | $N$ | Ra | Ta | Ro | Boundary conditions |
|---|---|---|---|---|---|
| RC1 | 128 | $10^5$ | $10^5$ | 1.0 | No-slip at all walls |
| RC2 | 128 | $10^5$ | $10^6$ | 0.316 | No-slip at all walls |
| RH | 128 | – | $10^6$ | 0.077 | No-slip at all walls |
| RCS | 128 | $10^5$ | $10^6$ | 0.316 | Constant stress at $x = 0$ and 1 |

## II. SIMULATION DETAILS

We use the finite difference code, SARAS [29,30], which solves the incompressible Navier-Stokes equations on a staggered grid and uses a multigrid solver for the pressure Poisson equation. We have validated SARAS for Rayleigh-Bénard convection (RBC) against the results of Wagner and Shishkina [31] for Pr = 0.786. Moreover, SARAS has also proven to be robust in simulating RBC for a wide range of Ra and Pr [32]. We use SARAS to simulate a Cartesian box of unit length along each direction, $L_x = L_y = L_z = 1$. Figure 2 shows a schematic diagram of the problem. Note that the rotation vector is along $-\hat{\mathbf{e}}_\mathbf{x}$, normal to the gravity, which acts along $-\hat{\mathbf{e}}_\mathbf{z}$; here $\hat{\mathbf{e}}_\mathbf{x}$ and $\hat{\mathbf{e}}_\mathbf{z}$ are unit vectors along the $x$ and $z$ directions, respectively. We solve the following equations for rotating Rayleigh-Bénard convection under the Boussinesq approximation [3]:

$$\frac{\partial \mathbf{u}}{\partial t} + (\mathbf{u}\cdot\boldsymbol{\nabla})\mathbf{u} = -\boldsymbol{\nabla} P + \left(\sqrt{\frac{\mathrm{Pr}}{\mathrm{Ra}}}\right)\nabla^2\mathbf{u} + T\hat{\mathbf{e}}_\mathbf{z} + \left(\sqrt{\frac{\mathrm{TaPr}}{\mathrm{Ra}}}\right)\hat{\mathbf{e}}_\mathbf{x}\times\mathbf{u}, \tag{1}$$

$$\frac{\partial T}{\partial t} + (\mathbf{u}\cdot\boldsymbol{\nabla})T = \frac{1}{\sqrt{(\mathrm{RaPr})}}\nabla^2 T, \tag{2}$$

$$\boldsymbol{\nabla}\cdot\mathbf{u} = 0. \tag{3}$$

Here $\mathbf{u}$ is the velocity field, $T$ is the temperature field, and $P$ is the pressure field. The above equations have been nondimensionalized using the free-fall velocity, $U = \sqrt{\beta g \Delta T L}$, as the velocity scale, $\Delta T = T_h - T_c$ as the temperature scale, and size of the domain $L$ (in each direction) as the length scale; here $T_h$ and $T_c$ are the temperatures of the hot and cold plates, respectively. The nondimensionalized parameters are Rayleigh number $\mathrm{Ra} = g\beta\Delta T L^3/\nu\kappa$, Prandtl number $\mathrm{Pr} = \nu/\kappa$, and Taylor number $\mathrm{Ta} = 4\Omega^2 L^4/\nu^2$. Here $\nu$ is the kinematic viscosity, $\beta$ is the thermal expansion coefficient, $g$ is gravitational acceleration, $\boldsymbol{\Omega} = -\Omega\hat{\mathbf{e}}_\mathbf{x}$ is the angular velocity, and $\kappa$ is the thermal diffusivity of the fluid, all of which are assumed constant for our simulations.

We perform four simulations, denoted as RH (rotating hydrodynamics with no-slip boundary condition), RC1 and RC2 (rotating convection with no-slip boundary condition), and RCS (rotating convection with constant stress boundary condition). All simulations are performed at a fixed Rayleigh number $\mathrm{Ra} = 10^5$ (except RH) and Prandtl number Pr = 1. For RC1 and RC2, $\mathrm{Ta} = 10^5$ and $10^6$, respectively (see Table I). The Rossby number is defined as $\mathrm{Ro} = \sqrt{\mathrm{Ra}/(\mathrm{TaPr})}$ [for RH, $\mathrm{Ro} = V_{\mathrm{rms}}/2\Omega L$, where $V_{\mathrm{rms}}$ is the root-mean-square (rms) velocity]. These parameters were chosen so that Ro is comparable to those in the spherical dynamo simulations discussed earlier (Ro for the simulation S0 in [12] is 0.4). The parameters for the simulation RH are similar to those for RC2, except that we switch off the buoyancy force for RH. Moreover, we employ a static conduction state (i.e., $\mathbf{u} = 0$ and $T$ varies linearly along the direction of gravity) as the initial condition for all the simulations except RH, in which we use the steady-state velocity field of RC2 as the initial condition. We start the simulation RH at $t = 490$ and wait till the signature of buoyancy in the velocity field almost fades away at $t = 496$. We use the velocity field at $t = 496$ of RH for our analysis. For RCS, we again use the same parameters as in RC2, except that we employ constant shear stress at the boundaries normal to the rotation axis (i.e., at $x = 0, 1$). The value of

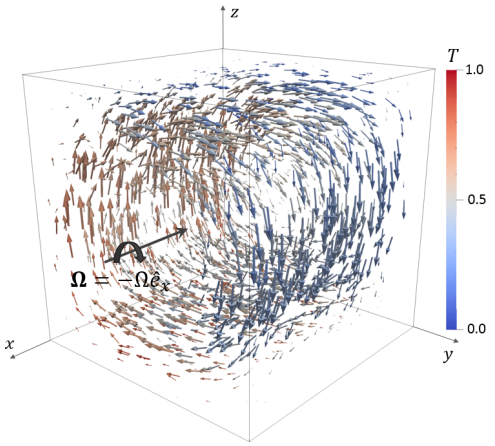


FIG. 3. Three-dimensional velocity vector field (colored with temperature) for RC2 showing dominance of cyclonic flow structure.

the nondimensional shear stress is set to $+3$ at $x = 0$ (where $\partial V_y/\partial x = 3$ and $\partial V_z/\partial x = 0$) and $-3$ at $x = 1$ (where $\partial V_y/\partial x = -3$, $\partial V_z/\partial x = 0$). These values are inspired by the dimensionless shear stress values in the geodynamo simulation S1 of Ranjan *et al.* [14].

## III. RESULTS AND DISCUSSION

We now present and analyze the results obtained from our simulations. We report the results for laminar, steady-state flow, i.e., when the field variables are not varying with time (except for RH, which is a decaying rotating flow). We also ensured that our results are independent of grid size by running the same cases at a higher resolution of $N = 256$ (see Fig. 14 in Appendix B).

Figure 3 shows the three-dimensional velocity vectors colored with temperature values for the run RC2. Here we observe a distinct cyclonic flow structure, which is typical in all our simulations. We notice the hot fluid rising and the cold fluid sinking in such a way that it forms a cyclonic structure of length scale comparable to the domain size. Such a dominant cyclonic flow has also been observed in earlier studies [18,19].

### A. Plane-averaged helicity

To identify the components of velocity and vorticity responsible for helicity generation and segregation, we analyze the three constituents of helicity, $V_x\omega_x$, $V_y\omega_y$, and $V_z\omega_z$. Figure 4 shows the variation of these helicity constituents and the total helicity ($\mathbf{u}\cdot\boldsymbol{\omega}$) along the $x$ axis for all four simulations. Note that these constituents and the total helicity are normalized by the maximum possible helicity $|\mathbf{u}||\boldsymbol{\omega}|$ at each point in the domain and then averaged in the $yz$ plane. We observe a clear segregation of helicity in the flow—negative near the wall with outward normal parallel to the rotation vector (near $x = 0$), and positive near the wall with outward normal antiparallel to the rotation vector (near $x = 1$). This corresponds to a negative (positive) helicity in the north (south), as seen in the spherical dynamo simulations results shown in Fig. 1. Note that all the constituents of helicity are contributing to the helicity segregation in the flow. Moreover, the helicity peak lies inside the Ekman boundary layer (the Ekman layer thickness is indicated in the figure). This observation points towards helicity generation inside the Ekman layer.

It is interesting to observe that for RC1 and RC2 the peaks of $V_x\omega_x$ and $V_y\omega_y$ are farther from the boundaries as compared to those of $V_z\omega_z$. RC1 exhibits an interesting distribution of helicity outside the Ekman layer—the average helicity is opposite to that near the walls. Note that the Coriolis force is weaker in RC1 (at $\mathrm{Ro} = 1$) as compared to RC2 ($\mathrm{Ro} \approx 0.3$). As expected from the Taylor-

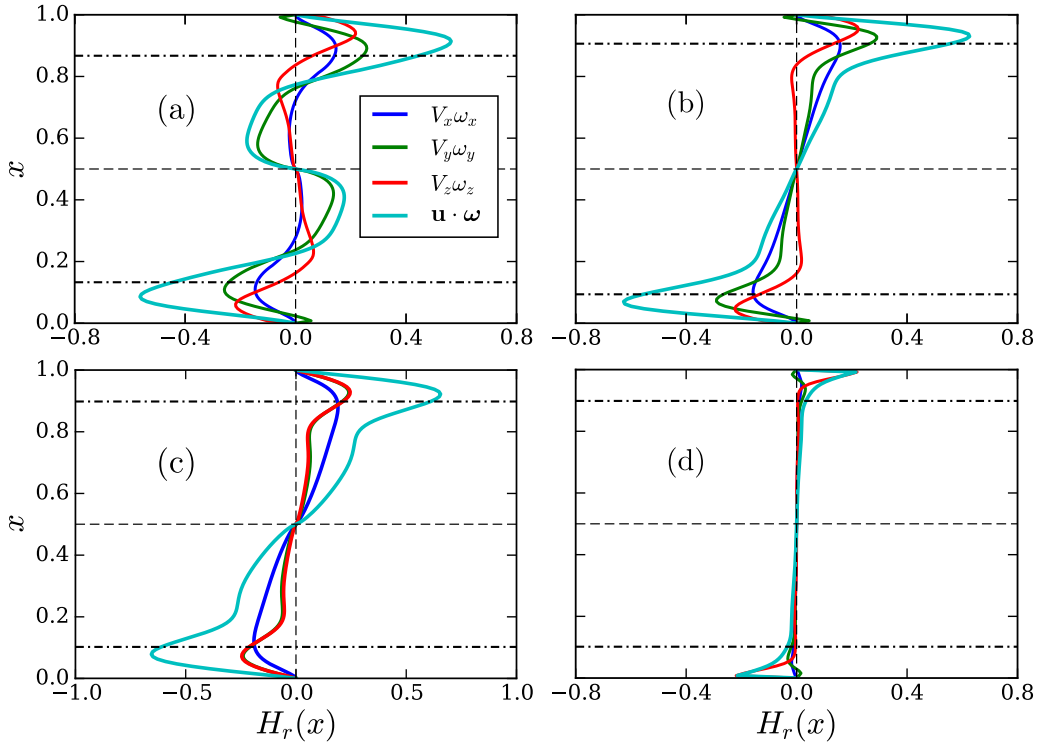


FIG. 4. Variation of the constituents of helicity normalized by the maximum possible helicity $|\mathbf{u}||\boldsymbol{\omega}|$ and averaged in the $yz$ plane ($H_r$) with $x$ for (a) RC1, (b) RC2, (c) RH, and (d) RCS. Horizontal dot-dashed lines represent the Ekman boundary layer thickness obtained from the velocity profile (see Appendix C). Note that the maximum value of the absolute helicity averaged in the $yz$ plane is 0.118, 0.133, 0.00025, and 0.149 for RC1, RC2, RH, and RCS, respectively.

Proudman theorem, stronger rotation leads to smaller flow variations along the rotation axis. This indicates that with stronger rotation (larger Ta, smaller Ro), variations in helicity also diminish along the rotation axis. We can also infer that the buoyancy force gives rise to an asymmetry between $V_y\omega_y$ and $V_z\omega_z$. Since buoyancy is absent in RH, $V_y\omega_y$ and $V_z\omega_z$ overlap each other. It is not surprising that the effect of buoyancy is observed mainly on $V_z\omega_z$, since gravity points along $-z$, but its effect on the helicity in the bulk is notable [compare Figs. 4(b) with Fig. 4(c)]. We also observe the expected helicity segregation in RCS, where a constant stress is applied at the walls with wall-normal parallel to the rotation axis, but the helicity is mostly concentrated close to the boundary and the peak magnitudes are very small.

### B. Helicity at different planes

We now use the plots of velocity and vorticity fields on different planes to further examine and explain the cause of helicity segregation. For the convenience of the readers, the locations of these planes are shown in Fig. 2(b). Figure 5 shows the contour plots of $V_x$, $\omega_x$, and $V_x\omega_x$, normalized by $V_{\rm rms}$, $\omega_{\rm rms}$, and $V_{\rm rms}\omega_{\rm rms}$ respectively, on the $yz$ plane at $x = 0.05$ (inside the Ekman layer). $V_{\rm rms}$ and $\omega_{\rm rms}$ are the rms values of the velocity and vorticity fields, respectively. The color plots are superimposed with velocity vectors denoted by arrows. Recall that the rotation vector (along $-\hat{\mathbf{e}}_\mathbf{x}$) points into the plane. For RC1, RC2 and RH, we see that $V_x$ is positive in the center of the plane, showing that fluid near the boundary is moving towards the bulk due to Ekman pumping (see the

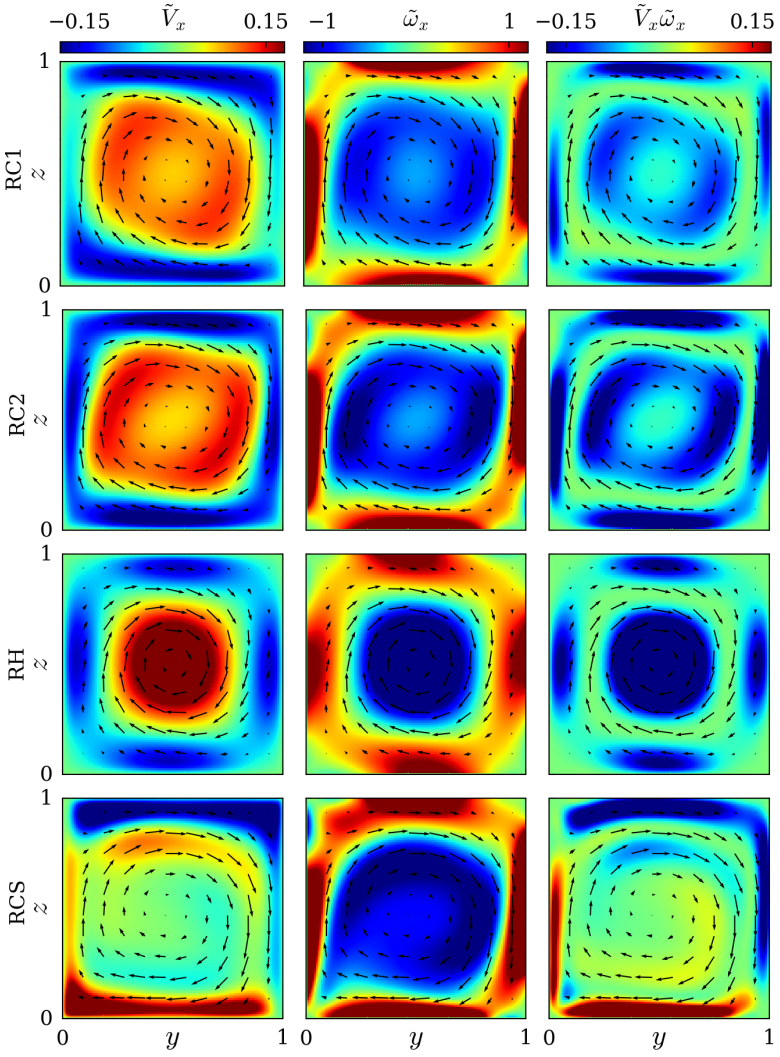


FIG. 5. Contour plots of normalized (by their rms values) $V_x$, $\omega_x$, and $V_x\omega_x$ (from left to right) superimposed with velocity vectors in the $yz$ plane at $x = 0.05$ for RC1 (first row), RC2 (second row), RH (third row), and RCS (fourth row).

first column of Fig. 5). Accordingly, $V_x$ near the side walls is negative due to the flow continuity. We also observe a dominant cyclonic flow structure, clearly visible in the region with negative $\omega_x$, outside the viscous boundary layers formed over the walls parallel to the rotation axis for all the runs (see the second column of Fig. 5). The positive values of $\omega_x$ (anticyclonic flow) observed close to the boundaries (perpendicular to the $y$ and $z$ axes) are due to the shear within the hydrodynamic boundary layer. $V_x$ is directed into the domain at the walls perpendicular to the rotation axis (positive near the $x = 0$ and negative near the $x = 1$ wall), whereas $\omega_x$ points along $-x$ all along the rotation axis due to the cyclonic flow. As a result, we obtain negative helicity at $x = 0.05$ (see third column of Fig. 5) and positive helicity at $x = 0.95$ (not shown here). For the case RH, both the velocity and vorticity magnitudes peak at the center and flow is perfectly symmetric, unlike that in RC1 and RC2 where $V_x$ and $\omega_x$ peak away from the center, and so the regions of high helicity in RC1 and RC2 are also shifted away from the rotation axis.

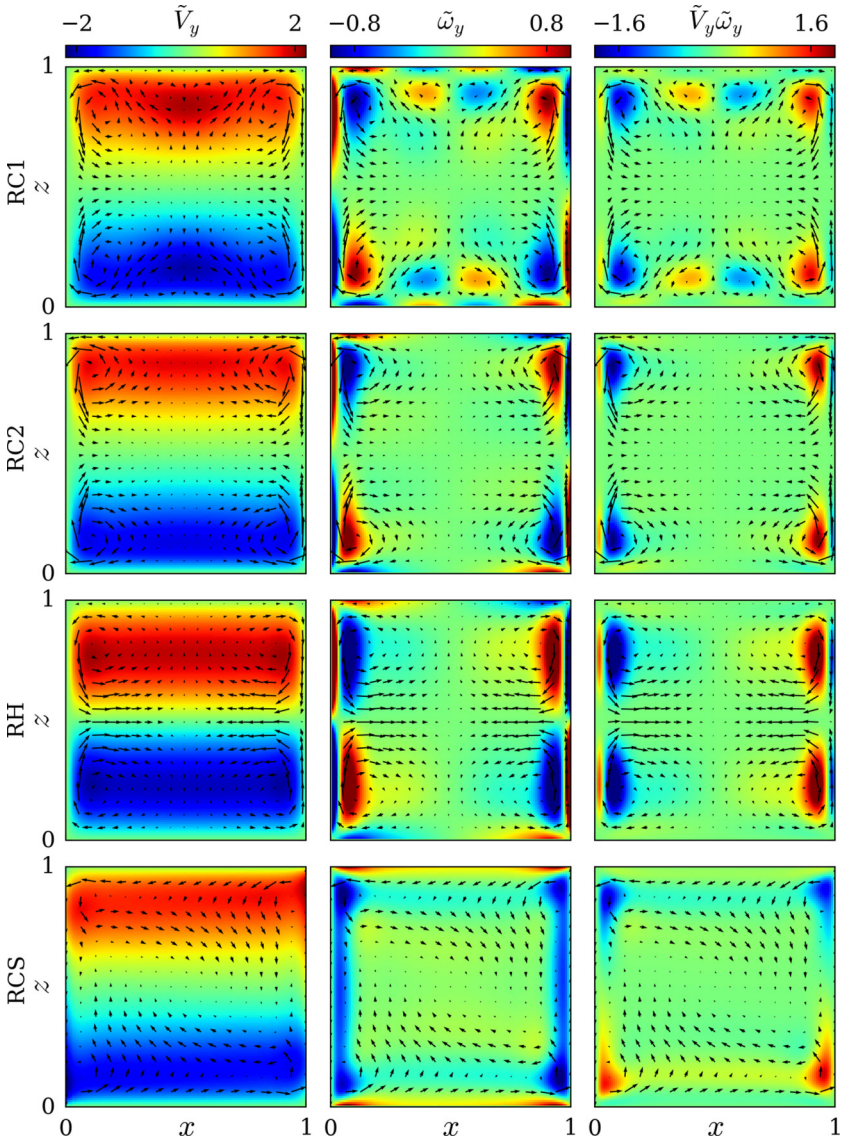


FIG. 6. Contour plots of normalized (by their rms values) $V_y$, $\omega_y$, and $V_y\omega_y$ (from left to right) superimposed with velocity vectors in the $xz$ plane at $y = 0.5$ for RC1 (first row), RC2 (second row), RH (third row), and RCS (fourth row).

Figure 6 shows similar quantities as in Fig. 5, plotted in the plane parallel to the rotation axis and gravity, i.e., the $xz$ plane, at $y = 0.5$. The vector plots in the runs RC1, RC2, and RH exhibit secondary rolls which are a clear signature of Ekman pumping (we use secondary flow structures and secondary rolls interchangeably in this paper). A zoomed view of the pair of secondary rolls is shown in Fig. 7. These rolls, present in the outer part of the Ekman boundary layer, pump the fluid away from the Ekman boundary layer towards the bulk. However, we notice a subtle difference between the rolls of RC2 and RH. In RH, the fluid pumped from the Ekman boundary layer into the bulk is mostly concentrated close to the rotation axis, whereas for RC2 it is more widely distributed. The secondary rolls also generate vorticity of opposite sign near the boundary (see the second column of Fig. 6). The cyclonic flow and Ekman pumping provide $V_y$ and $\omega_y$, respectively, in such a

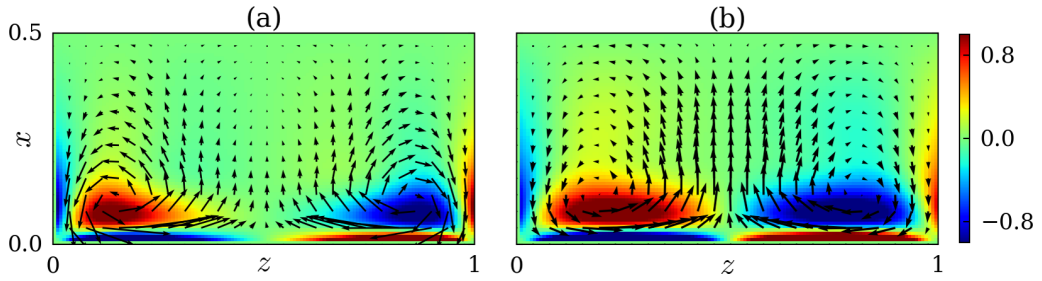


FIG. 7. Contour plot of normalized (by their rms value) $\omega_y$ superimposed with velocity vectors in the $xz$ plane at $y = 0.5$ for the run (a) RC2 and (b) RH. Signature of Ekman pumping is evident. Note that the vertical axis is along $x$ and horizontal along $z$.

way that their product exhibits negative (positive) helicity near the $x = 0$ ($x = 1$) wall (see the third column). Again, the regions of high $V_y\omega_y$ in RC1 and RC2 are located farther from the rotation axis. Due to the effect of buoyancy (note that gravity acts along $-z$), RC1 shows a region of weak $\omega_y$ of opposite sign outside the Ekman layer and close to the thermal walls. This explains the opposite helicity in the bulk regions of the flow for RC1 seen in Figs. 4 and 6.

Figure 8 shows contour plots in the $xy$ plane at $z = 0.5$, parallel to the rotation axis, perpendicular to gravity. Once again, we notice the signature of Ekman pumping as expected, though it is not as distinct as in Figs. 5 and 6 for RC1 and RC2. We speculate that this is due to the effect of buoyancy force. Recall that buoyancy also causes asymmetry between $V_y\omega_y$ and $V_z\omega_z$ [see Fig. 4(b)]. In the absence of buoyancy force for the run RH, the symmetry is established; $V_y\omega_y$ and $V_z\omega_z$ overlap each other, and the plots at the $y = 0.5$ and $z = 0.5$ planes become similar [see Fig. 4(c) and third row of Figs. 6 and 8]. Similar to Fig. 6, here the cyclonic flow and Ekman pumping provide $V_z$ and $\omega_z$ respectively, in such a way that their product exhibits negative (positive) helicity near the $x = 0$ ($x = 1$) wall.

In both Figs. 6 and 8, the sign of the vorticity components can also be understood by considering the velocity gradients along $x$ and invoking the Taylor-Proudman theorem ($\partial \boldsymbol{u}/\partial x \approx 0$). That is, we can consider $\partial V_z/\partial x$ (inferred from the first column of Fig. 8) to understand the distribution of $\omega_y$ (second column of Fig. 6). Similarly, $\partial V_y/\partial x$ (inferred from the first column of Fig. 6) can be considered for $\omega_z$ (second column of Fig. 8). As the rotation becomes stronger, as is the case for RC2, both these gradients become smaller and so do the vorticity components in the interior, thus leading to the same sign of helicity in the entire one-half of the box. Thus, we remark that the combined effect of Ekman pumping and the cyclonic flow is responsible for the helicity segregation in our simulations. For the anticyclones, which rotate opposite to the global rotation, the direction of Ekman pumping is reversed—the flow is towards the wall, also called Ekman suction [33]. Therefore, the same signs of helicity can be expected in anticyclones as well. In all three figures, Figs. 5, 6, and 8, the plots for RCS are markedly different from those for RC1, RC2, and RH. For example, compare $V_x$ in Fig. 5 and $\omega_y$, $\omega_z$ in Figs. 6 and 8. This indicates the importance of the boundary conditions and the presence of shear in different directions. To further reinforce this point, we also performed a simulation at the same parameters as in RC2, but with free-slip boundary conditions on the walls at $x = 0$ and $x = 1$. The helicity plots for this simulation (included in Appendix A) show no helicity generation near the boundaries, as expected. In RCS, the constant stress applied at the boundaries disrupts the secondary flows due to Ekman pumping (see Figs. 6 and 8), and as a result, the helicity values for RCS are reduced. Here nearly all of the helicity is generated by $V_z\omega_z$. The positive values of $\omega_z$ combine with the slightly more negative (positive) values of $V_z$ near the top-left (bottom-right) corners and result in the negative helicity at $x = 0$ and positive at $x = 1$. The asymmetry in $V_z$ seems to be important for this segregation. Also, the negligible contribution of $V_x\omega_x$ in the helicity segregation of RCS is due to the fact that there is a cancellation of helicity contributions from the top-bottom and left-right boundaries (see the last row

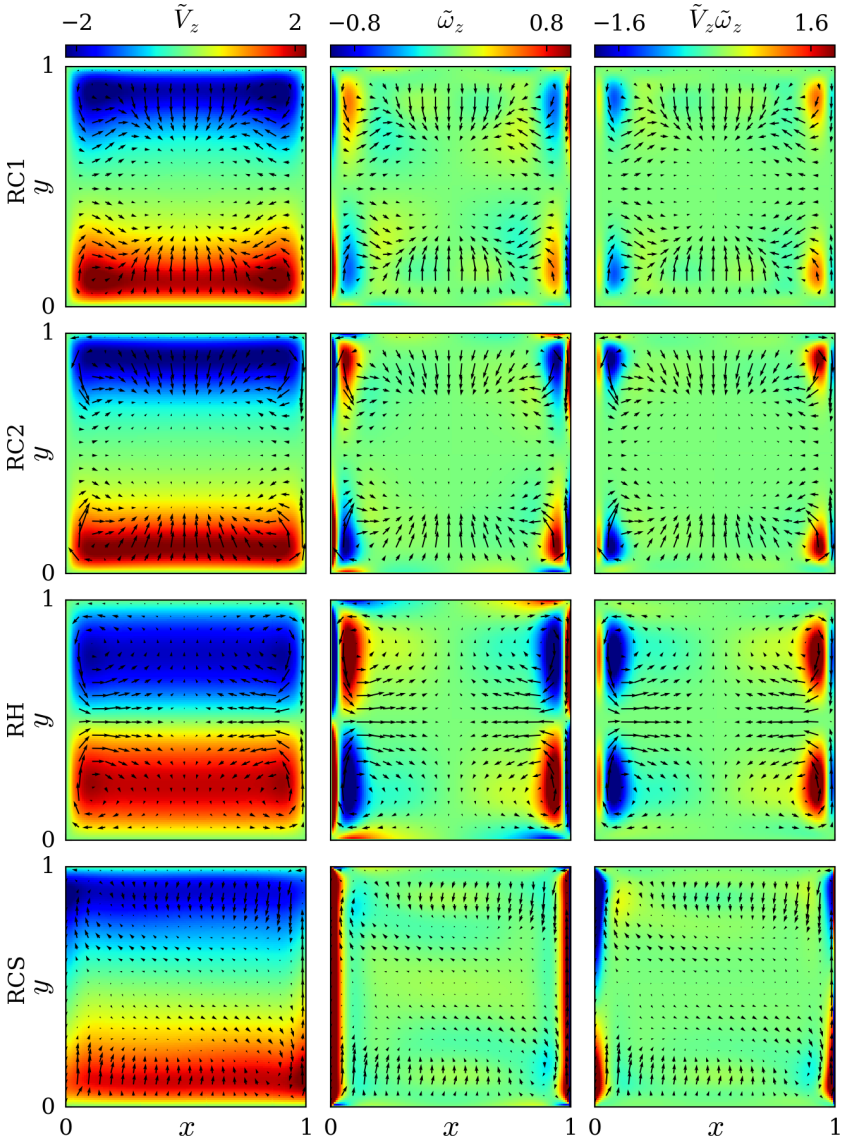


FIG. 8. Contour plots of normalized (by their rms values) $V_z$, $\omega_z$, and $V_z\omega_z$ (from left to right) superimposed with velocity vectors in the $xy$ plane at $z = 0.5$ for RC1 (first row), RC2 (second row), RH (third row), and RCS (fourth row).

of Fig. 5), much unlike the other cases. We find that for this case the (boundary-driven) flow and its associated helicity are localized near the boundaries. We also observe that by changing the sign of the applied stress on the two boundaries the helicity distributions do not change significantly (see the Supplemental Material [34]). The above explanations indicate that the helicity segregation in RCS is not directly associated with the flow structures due to Ekman pumping.

### C. Modal energy analysis

In the previous sections, we showed that two flow structures dominate the flow—cyclones and secondary flows due to Ekman pumping. Now, in order to quantify their importance in the

TABLE II. Modal energy of the dominant modes in $yz$ plane at $x = 0.5$ for RC1, RC2, RH, and RCS.

| Modes | RC1 energy % | RC2 energy % | RH energy % | RCS energy % |
|---|---|---|---|---|
| (1, 1) | 81.7 | 85.4 | 73.0 | 86.6 |
| (1, 3) | 5.00 | 1.50 | 10.9 | 2.70 |
| (1, 5) | 3.74 | 2.21 | 1.05 | 2.26 |
| (3, 1) | 0.01 | 0.11 | 10.8 | 0.51 |
| (5, 1) | 0.88 | 1.81 | 1.02 | 1.38 |

segregation of helicity, we analyze the energy contained in these flow structures using modal energy analysis. We expand the velocity fields in three planes $x = 0.5$, $y = 0.5$, and $z = 0.5$ using sine and cosine series. In the $yz$ plane at $x = 0.5$, the velocity field $V_y$ and $V_z$ are expanded as [35,36]

$$V_y = \sum_{mn} \hat{C}_{mn} \sin(m\pi y)\cos(n\pi z), \quad V_z = \sum_{mn} \hat{D}_{mn} \cos(m\pi y)\sin(n\pi z), \tag{4}$$

where $\hat{C}_{mn}$ and $\hat{D}_{mn}$ are the amplitudes of the velocity modes $(m, n)$. Similar expansion is used for the velocity fields in the other two planes. We compute the amplitudes $\hat{C}_{mn}$ and $\hat{D}_{mn}$ of the velocity modes $(m, n)$ using the orthogonal properties of the given functions, and then obtain the percentage energy of that particular mode in that plane.

Tables II, III, and IV show the percentage energy of the dominant structures in the flow at the $x = 0.5$, $y = 0.5$, and $z = 0.5$ planes, respectively. In the $yz$ plane at $x = 0.5$, we clearly see that the (1, 1) mode, which represents the cyclonic flow structures, dominates for RC1 (81.7%), RC2 (85.4%), RH (73.0%), and RCS (86.6%). For the velocity field in the $xz$ plane at $y = 0.5$, we see that the (2, 2) mode, which represents the secondary rolls due to Ekman pumping, contributes a significant amount of energy in the simulations RC1 (39.3%), RC2 (22.8%) and RH (53.7%). The modes representing the cyclonic flow [i.e., (1, 1)] and Ekman pumping [i.e., (2, 2)] together are responsible for the helicity generation and segregation in the flow, as discussed earlier. This is a novel result that has not been reported in the literature to the best of our knowledge. Note that in the $xy$ plane at $z = 0.5$, the mode (2, 2) does not contribute a significant amount of energy in the flow (for the case RC1 and RC2), most likely due to the presence of the buoyancy force. It is evident that in the run RH, the modal energy of the (2,2) mode contributes significantly (>50%) to the total energy in both the $xy$ and $xz$ planes. In fact, the energy values of the (2,2) mode in the $xz$ and $xy$ planes for the run RH are not very different.

### D. Force balance and helicity budget

We now analyze the force balance (for RC2 and RH) and the helicity budget (for RC1 and RC2) both inside and outside the Ekman layer. Figures 9 and 10 show the plots of the pressure gradient

TABLE III. Modal energy of the dominant modes in $xz$ plane at $y = 0.5$ for RC1, RC2, RH, and RCS.

| Mode | RC1 energy % | RC2 energy % | RH energy % | RCS energy % |
|---|---|---|---|---|
| (0, 2) | 0.59 | 1.49 | 0.58 | 15.1 |
| (1, 3) | 0.00 | 0.00 | 0.00 | 15.9 |
| (2, 2) | 39.3 | 22.8 | 53.7 | 0.11 |
| (2, 4) | 0.09 | 11.2 | 0.01 | 0.33 |
| (3, 1) | 0.00 | 0.00 | 0.00 | 14.5 |
| (4, 2) | 25.3 | 23.9 | 17.2 | 0.01 |
| (4, 4) | 17.5 | 6.30 | 0.04 | 0.09 |
| (5, 1) | 0.00 | 0.00 | 0.00 | 11.9 |
| (6, 2) | 1.72 | 11.4 | 7.23 | 0.06 |

TABLE IV. Modal energy of the dominant modes in $xy$ plane at $z = 0.5$ for RC1, RC2, RH, and RCS.

| Mode | RC1 energy % | RC2 energy % | RH energy % | RCS energy % |
|---|---|---|---|---|
| (0, 2) | 14.8 | 17.0 | 0.01 | 2.78 |
| (0, 4) | 21.2 | 30.2 | 0.05 | 23.6 |
| (1, 3) | 0.00 | 0.00 | 0.00 | 12.1 |
| (2, 0) | 27.5 | 12.3 | 10.4 | 0.05 |
| (2, 2) | 6.45 | 0.32 | 51.2 | 1.00 |
| (2, 4) | 5.54 | 2.99 | 0.01 | 0.17 |
| (4, 0) | 3.34 | 1.40 | 1.48 | 0.00 |
| (4, 2) | 4.75 | 7.18 | 18.8 | 0.23 |
| (6, 2) | 7.75 | 6.22 | 7.95 | 0.03 |

(including buoyancy force for RC2), Coriolis force, and viscous force at two $yz$ planes for RC2 and RH, respectively. The $yz$ plane in the first row (at $x = 0.5$) is far from the Ekman layer, and that in the second row (at $x = 0.05$) is inside the Ekman boundary layer. Vectors represent the respective force field directions, and the color represents the force magnitude. Note that the direction of the pressure gradient is towards the axis of rotation both inside and outside the Ekman layer, as would be expected for a cyclonic flow. Outside the Ekman layer (first row), it is evident that the pressure gradient (together with the buoyancy force for RC2) is balanced mainly by the Coriolis force, while the viscous force is comparatively negligible. This force balance between pressure gradient (with buoyancy force for RC2) and Coriolis force is given by the following equation:

$$-\nabla P + T\hat{\mathbf{e}}_\mathbf{z} + (1/\mathrm{Ro})\hat{\mathbf{e}}_\mathbf{x} \times \mathbf{u} \approx 0. \tag{5}$$

However, inside the Ekman layer (second rows in Figs. 9 and 10), we see that the viscous force is significant and contributes to the force balance. As expected, the nature of the viscous force is such

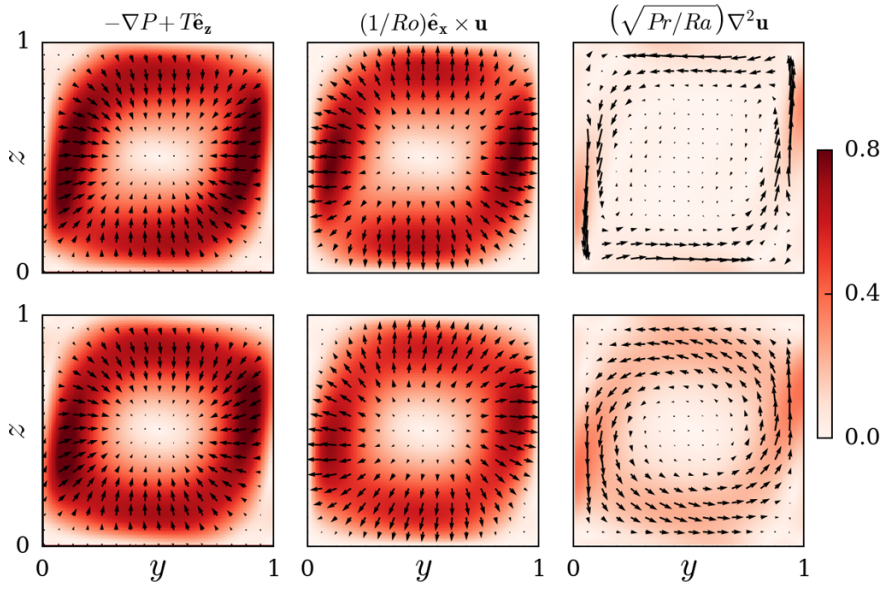


FIG. 9. Force balance between pressure gradient (including temperature) and Coriolis forces in the $yz$ plane at $x = 0.5$ (first row) and $x = 0.05$ (second row) for RC2. Vectors represent the respective force directions, and colors represent their magnitude. Direction of rotation is into the page.

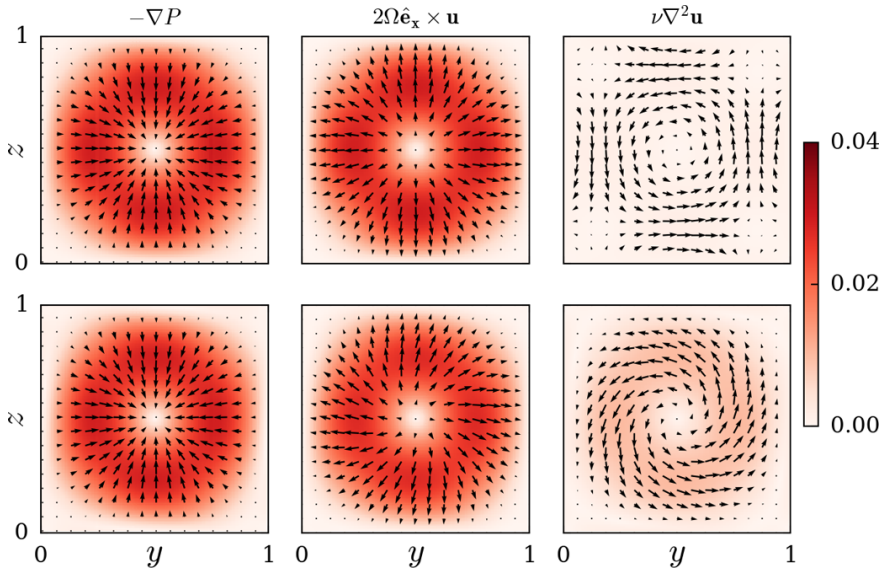


FIG. 10. Force balance between pressure gradient and Coriolis forces in the $yz$ plane at $x = 0.5$ (first row) and $x = 0.05$ (second row) for RH. Vectors represent the respective force directions, and colors represent their magnitude. Direction of rotation is into the page.

that it opposes the bulk cyclonic flow and the radially inward flow associated with Ekman pumping. The spiral nature of the flow inside the Ekman layer is clearly evident at this location, unlike that at $x = 0.5$. In this case, the pressure gradient (together with the buoyancy force for RC2) is balanced by both the Coriolis and viscous forces. This is the force balance inside the Ekman boundary layer for rotating flows, given by the following equation:

$$-\nabla P + T\hat{\mathbf{e}}_\mathbf{z} + (1/\mathrm{Ro})\hat{\mathbf{e}}_\mathbf{x} \times \mathbf{u} + \left(\sqrt{\frac{\mathrm{Pr}}{\mathrm{Ra}}}\right)\nabla^2\mathbf{u} = 0. \tag{6}$$

By contrasting the force balance between RC2 and RH (Figs. 9 and 10), we note that in the presence of buoyancy, an asymmetry in the force distribution in the $yz$ plane is introduced, since the fluid has an additional forcing along the $z$ direction. As the heated/cooled fluid is convected by the cyclone, it tends to rise and fall close to the sidewalls normal to the $y$ axis. Thus the buoyancy force makes the cyclonic flow stronger in regions closer to and along the walls normal to the $y$ axis (Figs. 5 and 9). This is seen in the form of stronger cyclonic velocities parallel to the $z$ axis and slightly weaker velocities parallel to the $y$ axis for the case RC2. The concentrated circular cyclone of the case RH (Figs. 5 and 10) takes an annular form in the presence of buoyancy with a "near-dead" flow region at the center. Accordingly, the regions of large radial pressure gradients and high Coriolis forces (and consequently, the regions of significant Ekman pumping) also migrate away from the axis of rotation (Fig. 9).

We also analyze the various sources of helicity generation using the following helicity budget equation, which can derived by obtaining $\boldsymbol{\omega} \cdot \partial\mathbf{u}/\partial t + \mathbf{u} \cdot \partial\boldsymbol{\omega}/\partial t$ [14]:

$$\frac{\partial h}{\partial t} = -\nabla \cdot \mathbf{F} + h_T + h_\nu, \tag{7}$$

where we have ignored the advection term for small Rossby number. Here

$$\mathbf{F} = \frac{1}{\mathrm{Ro}}\mathbf{u}^2\hat{\mathbf{e}}_\mathbf{x} + \frac{1}{\mathrm{Ro}}\mathbf{u} \times \hat{\mathbf{e}}_\mathbf{x} \cdot \nabla\mathbf{a} + p\boldsymbol{\omega},$$

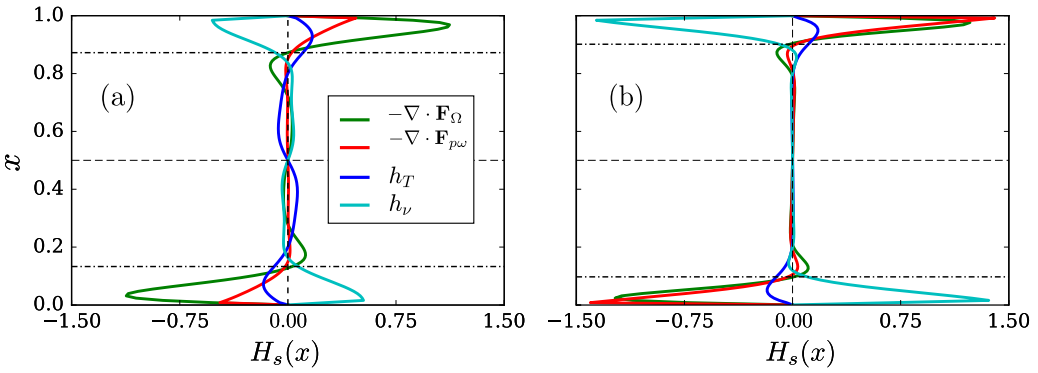


FIG. 11. Variation of the helicity flux and helicity source terms averaged in the $yz$ plane ($H_s$) along the rotation axis ($x$ direction) for (a) RC1, and (b) RC2. Note that $-\nabla\cdot\mathbf{F}_\Omega$ and $-\nabla\cdot\mathbf{F}_{p\omega}$ terms represent the helicity flux due to Coriolis force and pressure-vorticity force, respectively, whereas $h_T$ and $h_\nu$ terms represent the helicity generation due to buoyancy force and viscous force, respectively. Dot-dashed lines represent the Ekman boundary layer thickness.

$$h_T = \boldsymbol{\omega}\cdot T\hat{\mathbf{e}}_\mathbf{z} + \mathbf{u}\cdot(\nabla T\times\hat{\mathbf{e}}_\mathbf{z}),$$
$$h_\nu = \sqrt{\frac{\mathrm{Pr}}{\mathrm{Ra}}}(\boldsymbol{\omega}\cdot\nabla^2\mathbf{u} + \mathbf{u}\cdot\nabla^2\boldsymbol{\omega}).$$

$\mathbf{F}$ represents the flux of helicity, and $h_T$ and $h_\nu$ are the sources of helicity due to buoyancy and viscous forces, respectively. The vector $\mathbf{a}$ in the expression for $\mathbf{F}$ is a solenoidal vector potential for $\mathbf{u}$ ($\mathbf{u}=\nabla\times\mathbf{a}$, $\nabla\cdot\mathbf{a}=0$). We denote the helicity fluxes due to Coriolis and pressure-vorticity forces as $\mathbf{F}_\Omega = (1/\mathrm{Ro})\mathbf{u}^2\hat{\mathbf{e}}_\mathbf{x}$ and $\mathbf{F}_{p\omega} = p\boldsymbol{\omega}$, respectively. For a geostrophic flow, the contribution of the second term in $\mathbf{F}$ towards helicity segregation is expected to be negligible [14], and, therefore, we ignore it in this analysis.

In Fig. 11 we plot the variation of $-\nabla\cdot\mathbf{F}_\Omega$, $-\nabla\cdot\mathbf{F}_{p\omega}$, $h_T$, and $h_\nu$ (averaged in the $yz$ plane) along the rotation axis. We note that there is a significant helicity flux both from the pressure-vorticity term ($-\nabla\cdot\mathbf{F}_{p\omega}$) and from the Coriolis term ($-\nabla\cdot\mathbf{F}_\Omega$). This generation and transport are similar to the mechanism proposed by Deusebio and Lindborg [37] where the pressure-vorticity flux leads to the generation of helicity, analogous to the generation of kinetic energy by pressure work. Buoyancy also contributes to helicity segregation, but its contribution is lower than that of Coriolis and pressure-vorticity forces in our simulations. It is interesting to note that $h_T$ was larger near the boundaries even in the simulations of Ranjan *et al.* [14] and is likely to dominate near the boundaries in the S0 simulation of Schaeffer *et al.* [12]. Note also that the sign of helicity segregation due to the viscous force is opposite to that of Coriolis and buoyancy forces, once again in agreement with the observations in the dynamo simulations of Ranjan *et al.* [14]. Another interesting observation, in particular for the case RC2, is that the helicity flux due to pressure-vorticity force ($\mathbf{F}_{p\omega}$) is approximately balanced by the helicity due to the viscous force ($h_\nu$).

## IV. DISCUSSION AND CONCLUSIONS

In this work, we numerically investigated the role of Ekman pumping in the segregation of kinetic helicity. Our domain of interest is a Cartesian box with the rotation axis perpendicular to gravity, inspired by the equatorial regions in the Earth's core. We performed simulations at fixed Rayleigh and Prandtl numbers for two values of the Taylor number, $\mathrm{Ta}=10^5$ and $10^6$, and two boundary conditions—no-slip and fixed stress on the walls normal to the rotation axis (see Table I). At large Ta (strong rotation), our results show that the normalized helicity is negative in the regions closer to $x=0$ and positive in the regions closer to $x=1$ (recall that $x=0$ and $x=1$ correspond to the

vertical walls normal to the rotation axis). In spherical dynamo simulations, such as those shown in Fig. 1, these half-volumes correspond to the north and south of the equator, respectively. Moreover, we found that the peak helicity magnitude occurs inside the Ekman layers, indicating that the helicity is generated here and transported to the bulk regions. Analysis of the helicity budget shows that the Coriolis and the pressure-vorticity fluxes contribute to the observed segregation of helicity.

We also analyzed the three constituents of helicity, $V_x\omega_x$, $V_y\omega_y$, and $V_z\omega_z$, to investigate the cause of helicity segregation. By observing the distributions of these constituents at different planes in the domain, we concluded that Ekman pumping and cyclonic structures are together responsible for this helicity segregation. We found that near the Ekman boundary layer, $V_x$, $\omega_y$, and $\omega_z$ are generated by Ekman pumping, whereas the cyclonic flow drives $V_y$, $V_z$, and $\omega_x$ (recall that the rotation vector is along $-x$). The coupled effect of these two phenomena leads to the observed helicity segregation. The helicity magnitudes were found to be smaller for the constant stress simulations and localized very close to the wall, as compared to the no-slip simulations. With an increase in Ta, the velocity gradients parallel to the rotation axis decrease, as expected from the Taylor-Proudman theorem. Therefore, with an increase in Ta and for lower values of Ra/Ta, the average helicity in the bulk regions of the box (in the same half) has the same sign as the helicity in the Ekman layers. Our results suggest that helicity in the dynamo simulations at large Ta but small $\mathrm{Ra}/\mathrm{Ra}_{\mathrm{critical}}$ arises due to Ekman pumping. We also presented a modal energy analysis to quantify the relative energies of the dominant structures in the flow and found that the secondary rolls [represented by the mode $(2, 2)$] generated by Ekman pumping to be an important flow feature. This is the first numerical demonstration of helicity segregation by Ekman pumping in a simple box geometry and is in agreement with the predictions by Busse [16] and Olson *et al.* [8].

The role of buoyancy in helicity generation and segregation is an important topic of great interest to geophysical and astrophysical community. For instance, in the context of solar dynamos, Duarte *et al.* [38] reported helicity inversion due to buoyancy gradients. In a recent letter, Agoua *et al.* [39] found spontaneous helicity generation and reversal in sign due to buoyancy effects in quasi-two-dimensional (anisotropic) turbulence. In this work, we observed that buoyancy plays an important role in the migration of the secondary rolls associated with the Ekman pumping (and so the helicity concentration) away from the rotation axis. In the future, we plan to vary the Rayleigh number to investigate in detail the effect of buoyancy force. We will also investigate other configurations where gravity and rotation are inclined at different angles to each other, as well as the case where a mean magnetic field is present.

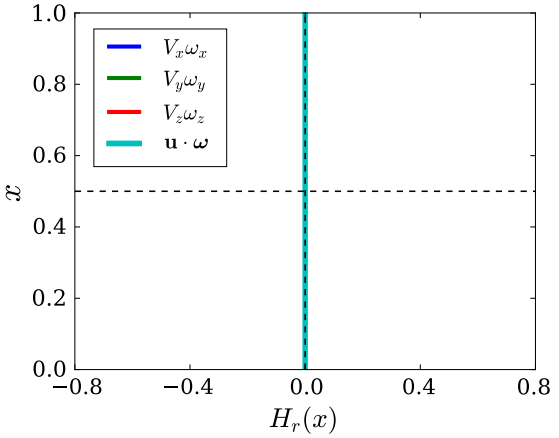


FIG. 12. Variation of the constituents of helicity normalized by maximum possible helicity $|\mathbf{u}||\boldsymbol{\omega}|$ and averaged in the $yz$ plane ($H_r$) with $x$ for free-slip boundary conditions on the walls perpendicular to the rotation vector.

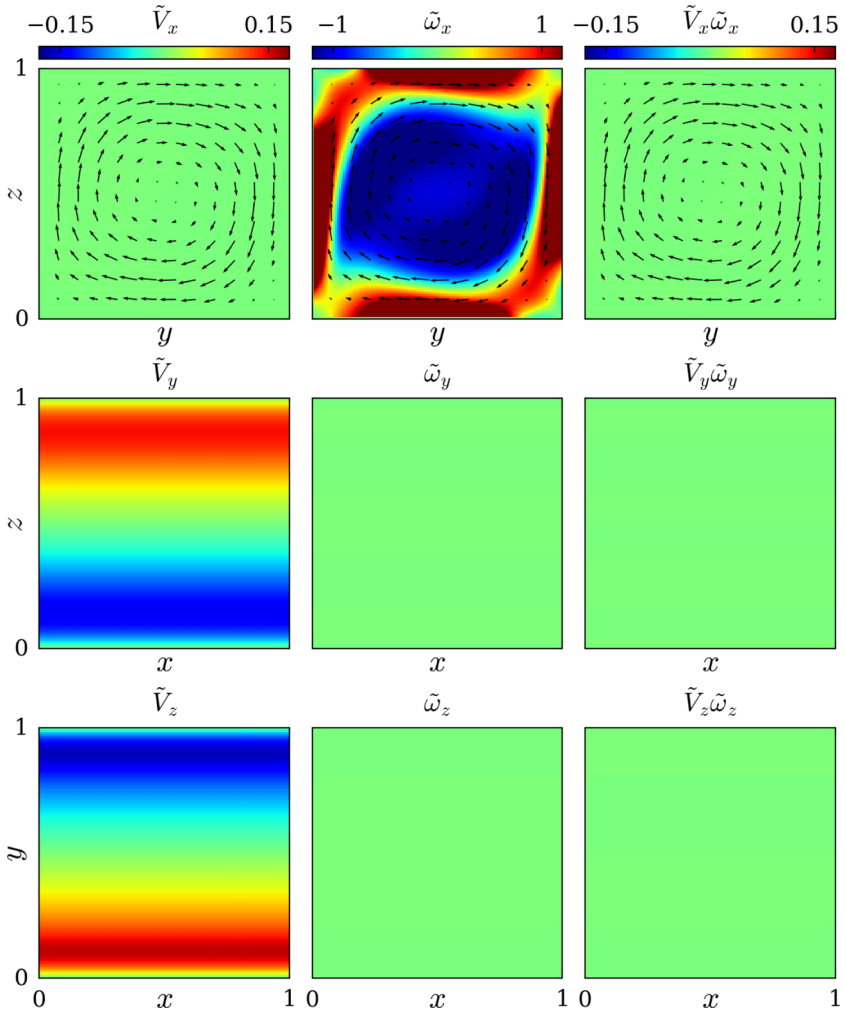


FIG. 13. Contour plots of normalized (by their rms values) $V_x$, $\omega_x$, and $V_x\omega_x$ in the $yz$ plane at $x = 0.05$ (first row), $V_y$, $\omega_y$, and $V_y\omega_y$ in the $xz$ plane at $y = 0.5$ (second row), and $V_z$, $\omega_z$, and $V_z\omega_z$ in the $xy$ plane at $z = 0.5$ (third row) for free-slip BCs on walls perpendicular to the rotation vector ($x$ direction).

## ACKNOWLEDGMENTS

We thank Roshan Samuel for his help in editing the code and providing valuable suggestions for the manuscript. We performed our simulations on the High Performance Computing facility at IIT Kanpur. Access to computational facility was partially supported by Science and Engineering Research Board (SERB), Department of Science & Technology, Government of India, Project no. SRG/2019/001037.

## APPENDIX A: FREE-SLIP BOUNDARY CONDITION

For comparison, we also include the results for free-slip boundary conditions. We impose free-slip boundary condition on the walls at $x = 0$ and $x = 1$ while retaining no-slip boundary condition on the other walls. Moreover, we use the same parameters as in RC2. Figure 12 shows there is negligible helicity generation for free-slip BCs. To explain it, we present Fig. 13. Due to the

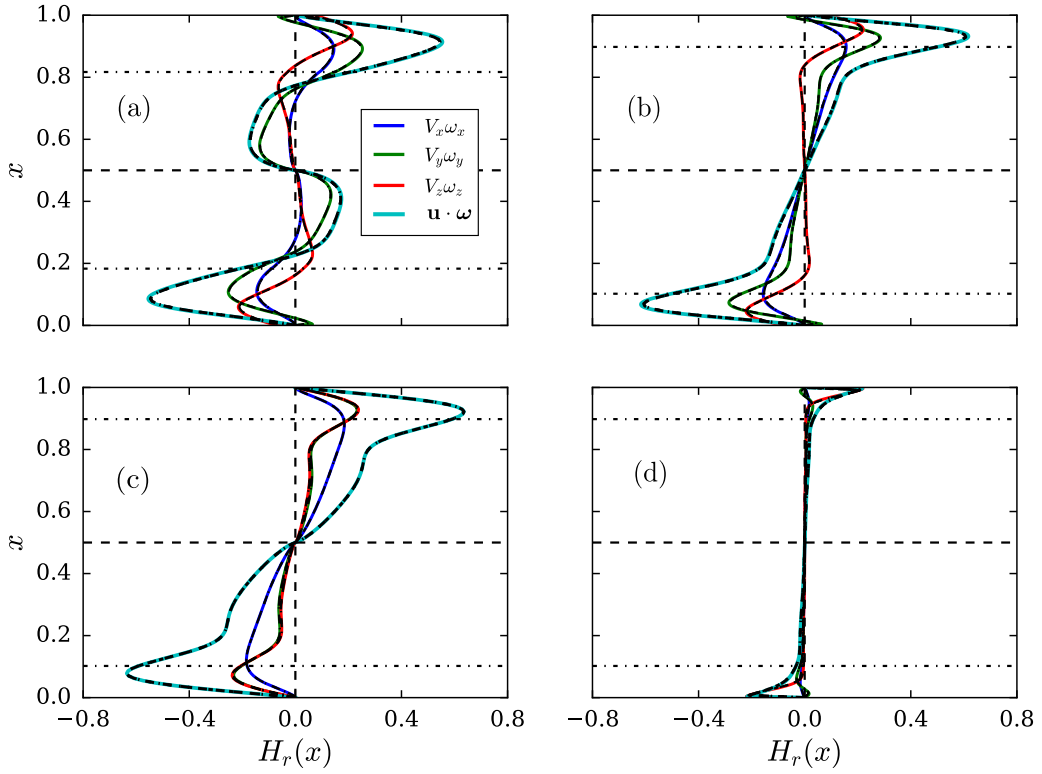


FIG. 14. Variation of the constituents of helicity normalized by maximum possible helicity $|\mathbf{u}||\boldsymbol{\omega}|$ and averaged in the $yz$ plane ($H_r$) with $x$ for (a) RC1, (b) RC2, (c) RH, and (d) RCS. Continuous and dot-dashed lines represent results with $N = 128$ and $N = 256$, respectively.

absence of Ekman pumping for the free-slip BC, $V_x$, $\omega_y$, and $\omega_z$ are not generated, and hence all the constituents of helicity become zero.

## APPENDIX B: GRID INDEPENDENCE

To ensure that our results are independent of grid size, we have also performed simulations using $N = 256$ grid points for the same parameters. In Fig. 14 continuous ($N = 128$) and the corresponding dot-dashed ($N = 256$) lines are overlapping each other, showing that all the spatial scales present in our simulations are fully resolved for the grid $N = 128$.

## APPENDIX C: VELOCITY PROFILE

To obtain the velocity (or Ekman) boundary layer thickness, we plot Fig. 15 for the variation of the normalized velocity averaged in the $yz$ plane ($V_{yz} = \langle\sqrt{V_y^2 + V_z^2}\rangle_{yz}$) with $x$. The velocity boundary layer thickness for RC1, RC2, and RH is defined as the distance from the wall to the maximum of the velocity. The velocity profile of RCS, however, is very different in nature from that of others. So we use $\delta_E \approx 2.284\sqrt{\nu/\Omega}$ to give a reference value of velocity boundary layer thickness for RCS. At this location variation of $V_{yz}$ with $x$ for RCS becomes negligible (less than 4% of the maximum variation at the boundary). Note that $\delta_E \approx 2.284\sqrt{\nu/\Omega}$ for Ekman layer thickness is obtained using

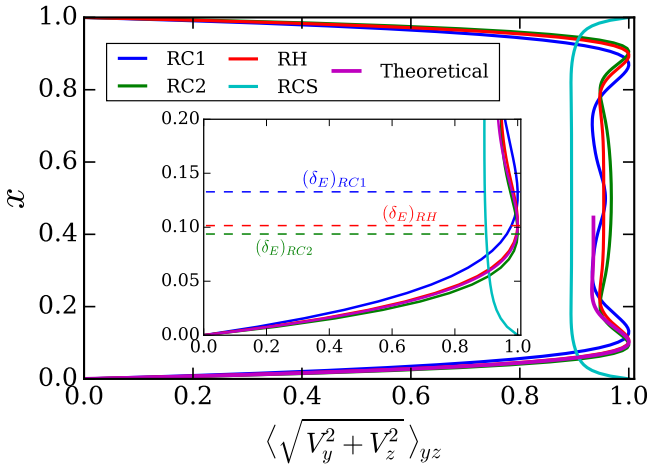


FIG. 15. Variation of the normalized velocity averaged in the $yz$ plane with $x$. Inset shows zoomed view near the boundary. $(\delta_E)_{\mathrm{RC1}} = 0.133$, $(\delta_E)_{\mathrm{RC2}} = 0.094$, and $(\delta_E)_{\mathrm{RH}} = 0.102$ indicate the velocity boundary layer thickness for RC1, RC2, and RH, respectively. Theoretical velocity profile is obtained using the equation given in Kundu *et al.* [40].

the velocity equation given in Kundu *et al.* [40]. Also, this estimate of the Ekman layer thickness matches quite well RH (rotating hydrodynamic case) where $(\delta_E)_{RH} \approx 2.284\sqrt{\nu/\Omega} \approx 0.102$.


[1] H. K. Moffatt, *Magnetic Field Generation in Electrically Conducting Fluids* (Cambridge University Press, Cambridge, 1978).

[2] A. D. Gilbert, U. Frisch, and A. Pouquet, Helicity is unnecessary for alpha effect dynamos, but it helps, Geophys. Astrophys. Fluid Dyn. **42**, 151 (1988).

[3] M. K. Verma, *Physics of Buoyant Flows: From Instabilities to Turbulence* (World Scientific, Singapore, 2018).

[4] M. Y. Reshetnyak, Evolution of helicities in dynamo problems, Dokl. Phys. **60**, 283 (2015).

[5] F. Plunian, R. Stepanov, and P. Frick, Shell models of magnetohydrodynamic turbulence, Phys. Rep. **523**, 1 (2012).

[6] H. K. Moffatt and A. B. Tsinober, Helicity in laminar and turbulent flow, Annu. Rev. Fluid Mech. **24**, 281 (1992).

[7] E. Parker, Hydromagnetic dynamo models, Astrophys. J. **122**, 293 (1955).

[8] P. Olson, U. Christensen, and G. A. Glatzmaier, Numerical modeling of the geodynamo: Mechanisms of field generation and equilibration, J. Geophys. Res.: Solid Earth **104**, 10383 (1999).

[9] P. A. Davidson, The dynamics and scaling laws of planetary dynamos driven by inertial waves, Geophys. J. Int. **198**, 1832 (2014).

[10] M. Y. Reshetnyak, Hydrodynamic helicity in Boussinesq-type models of the geodynamo, Izv. Phys. Solid Earth **42**, 449 (2006).

[11] B. Sreenivasan and C. A. Jones, Helicity generation and subcritical behaviour in rapidly rotating dynamos, J. Fluid Mech. **688**, 5 (2011).

[12] N. Schaeffer, D. Jault, H.-C. Nataf, and A. Fournier, Turbulent geodynamo simulations: A leap towards Earth's core, Geophys. J. Int. **211**, 1 (2017).

[13] B. Sreenivasan and S. Kar, Scale dependence of kinetic helicity and selection of the axial dipole in rapidly rotating dynamos, Phys. Rev. Fluids **3**, 093801 (2018).

[14] A. Ranjan, P. A. Davidson, U. R. Christensen, and J. Wicht, On the generation and segregation of helicity in geodynamo simulations, Geophys. J. Int. **221**, 741 (2020).
[15] F. H. Busse, Generation of planetary magnetism by convection, Phys. Earth Planet. Interiors **12**, 350 (1976).
[16] F. H. Busse, A model of the geodynamo, Geophys. J. Int. **42**, 437 (1975).
[17] H. Kitauchi, K. Araki, and S. Kida, Flow structure of thermal convection in a rotating spherical shell, Nonlinearity **10**, 885 (1997).
[18] A. Kageyama, K. Watanabe, and T. Sato, Simulation study of a magnetohydrodynamic dynamo: Convection in a rotating spherical shell, Phys. Fluids B **5**, 2793 (1993).
[19] A. Kageyama and T. Sato, Generation mechanism of a dipole field by a magnetohydrodynamic dynamo, Phys. Rev. E **55**, 4617 (1997).
[20] F. H. Busse, Convective flows in rapidly rotating spheres and their dynamo action, Phys. Fluids **14**, 1301 (2002).
[21] P. Olson, *Core Dynamics: Treatise on Geophysics* (Elsevier, 2007).
[22] N. Schaeffer and P. Cardin, Quasi-geostrophic kinematic dynamos at low magnetic Prandtl number, Earth Planet. Sci. Lett. **245**, 595 (2006).
[23] P. A. Davidson and A. Ranjan, Planetary dynamos driven by helical waves—II, Geophys. J. Int. **202**, 1646 (2015).
[24] P. A. Davidson and A. Ranjan, On the spatial segregation of helicity by inertial waves in dynamo simulations and planetary cores, J. Fluid Mech. **851**, 268 (2018).
[25] J. Aurnou, M. Calkins, J. Cheng, K. J. Julien, E. King, D. Nieves, K. Soderlund, and S. Stellmach, Rotating convective turbulence in earth and planetary cores, Phys. Earth Planet. Interiors **246**, 52 (2015).
[26] U. R. Christensen, Zonal flow driven by strongly supercritical convection in rotating spherical shells, J. Fluid Mech. **470**, 115 (2002).
[27] U. R. Christensen, P. L. Olson, and G. A. Glatzmaier, Numerical modelling of the geodynamo: A systematic parameter study, Geophys. J. Int. **138**, 393 (1999).
[28] R. K. Yadav, T. Gastine, and U. R. Christensen, Scaling laws in spherical shell dynamos with free-slip boundaries, Icarus **225**, 185 (2013).
[29] M. K. Verma, R. Samuel, S. Chatterjee, S. Bhattacharya, and A. Asad, Challenges in fluid flow simulations using exascale computing, SN Comput. Sci. **1**, 2661 (2020).
[30] R. Samuel, S. Bhattacharya, A. Asad, S. Chatterjee, M. K. Verma, R. Samtaney, and S. F. Anwer, A general-purpose PDE solver for fluid dynamics, J. Open Source Softw. **6**, 2095 (2021).
[31] S. Wagner and O. Shishkina, Aspect-ratio dependency of Rayleigh-Bénard convection in box-shaped containers, Phys. Fluids **25**, 085110 (2013).
[32] S. Bhattacharya, M. K. Verma, and R. Samtaney, Prandtl number dependence of the small-scale properties in turbulent Rayleigh-Bénard convection, Phys. Rev. Fluids **6**, 063501 (2021).
[33] E. Dormy and A. M. Soward, *Mathematical Aspects of Natural Dynamos* (Chapman & Hall/CRC, Boca Raton, FL, 2007).
[34] See Supplemental Material at http://link.aps.org/supplemental/10.1103/PhysRevFluids.7.034801 for the other boundary conditions of RCS case.
[35] M. Chandra and M. K. Verma, Flow Reversals in Turbulent Convection via Vortex Reconnections, Phys. Rev. Lett. **110**, 114503 (2013).
[36] M. Chandra and M. K. Verma, Dynamics and symmetries of flow reversals in turbulent convection, Phys. Rev. E **83**, 067303 (2011).
[37] E. Deusebio and E. Lindborg, Helicity in the Ekman boundary layer, J. Fluid Mech. **755**, 654 (2014).
[38] L. Duarte, J. Wicht, M. K. Browning, and T. Gastine, Helicity inversion in spherical convection as a means for equatorward dynamo wave propagation, Mon. Not. R. Astron. Soc. **456**, 1708 (2016).
[39] W. Agoua, B. Favier, A. Delache, A. Briard, and W. J. T. Bos, Spontaneous generation and reversal of helicity in anisotropic turbulence, Phys. Rev. E **103**, L061101 (2021).
[40] P. K. Kundu, I. M. Cohen, and D. R. Dowling, *Fluid Mechanics*, 6th ed. (Academic Press, San Diego, 2015).